Materials & Design 261 (2026) 115314

Contents lists available at ScienceDirect

Materials & Design

journal homepage: www.elsevier.com/locate/matdes

Phase-field modeling of microstructure formation in FePt-C nanogranular films sputtered on MgO

Yusuke Matsuoka [a,*], Machiko Ode [a], Taichi Abe [a], Toshiyuki Koyama [a], Yukiko K. Takahashi [a,b]

[a] National Institute for Materials Science, Sengen, Tsukuba 305-0047, Japan
[b] Research Institute of Electrical Communication, Tohoku University, Sendai 980-8577, Japan

ARTICLE INFO

Keywords:
Phase-field method
Simulation
$L1_0$ FePt film
Magnetic thin films
Heat-assisted magnetic recording

ABSTRACT

This study investigates microstructure formation in FePt-C nanogranular films deposited on MgO substrates during sputtering using the phase-field method, aiming to identify the key factors promoting the creation of an island-like microstructure, which is essential for the high recording density required in hard disk drives. Simulations reproduced the growth and coarsening of FePt grains, indicating that elastic-strain energy relaxation contributes significantly toward the formation of well-isolated FePt islands. The addition of C as a segregant shifts the position of the atoms supplied by sputtering closer to the top surface of the FePt grains, promoting their vertical growth. Furthermore, the film microstructure varies with the sputtering rate: lower rates result in coarser structures, whereas higher rates result in finer structures, albeit at the risk of grain coalescence. The results of this study suggest that the final microstructure is determined by the interplay of energetic and kinetic factors, specifically the interfacial and elastic strain energies and the diffusion and sputtering rates. These findings will enable the formulation of fabrication strategies for optimal high-performance FePt magnetic recording films.

1. Introduction

Rapid advancements in artificial intelligence (AI) technology have led to an unprecedented increase in the amount of data handled by humans, resulting in increased demand for data centers. The significant power consumption of these data centers is emerging as a critical issue. Global data-center power consumption is predicted to reach 945 TWh by 2030, which is more than double that of 2024 [1]. Therefore, improving energy efficiency is a critical issue that should be addressed urgently. Because most data are stored on hard disk drives (HDDs), improving their energy efficiency per unit capacity is crucial for reducing the overall data-center power consumption. Consequently, the development of next-generation HDDs is being actively pursued at present.

Heat-assisted magnetic recording (HAMR) media using $L1_0$-ordered FePt as a magnetic recording medium are emerging as promising solutions to the data center power-consumption issue [2]. The strong magnetic anisotropy of $L1_0$-FePt ensures high magnetic stability for small grains, enabling the magnetic recording layer to show a high grain density. This improves the magnetic recording density and power efficiency per unit capacity of the device. Efforts are currently underway to manufacture systems with a recording density of 4 TB/in^2; such systems are required to exhibit an FePt grain density of 24T/in^2 [2].

The magnetic recording layer in HAMR HDDs consists of an FePt-X film comprising uniformly dispersed FePt grains surrounded by a segregant (X) [3]. FePt-X film fabrication typically involves deposition on MgO substrates via sputtering [3,4]. The microstructure of a system with high recording density shows certain specific characteristics, such as a small FePt grain diameter (D), high grain height (h) to grain diameter aspect ratio (h/D), and high grain-size uniformity (σ). For instance, a system with a recording density of 4 TB/in^2 must exhibit $D <$ 4.3 nm, $h/D > 1.6$, and $\sigma <$ 10–15 % as well as the good $L1_0$ ordering of FePt grains and an out-of-plane [001] texture [2,5].

Multiple studies have attempted to meet these requirements by focusing on optimizing the sputtering process [6–9] or exploring new substrate [10–15] and segregant [3,4,6,12,16–18] materials. Among them, a study by Perumal et al. represents a major breakthrough in this field; it reports that co-sputtering FePt and C on MgO substrates results in fine and uniform FePt nanogranular films [3]. Subsequent studies

* Corresponding author.
E-mail addresses: MATSUOKA.yusuke@nims.go.jp (Y. Matsuoka), ODE.Machiko@nims.go.jp (M. Ode), ABE.Taichi@nims.go.jp (T. Abe), KOYAMA.Toshiyuki@nims.go.jp (T. Koyama), TAKAHASHI.Yukiko@nims.go.jp (Y.K. Takahashi).

https://doi.org/10.1016/j.matdes.2025.115314
Received 2 September 2025; Received in revised form 7 November 2025; Accepted 9 December 2025
Available online 10 December 2025

have investigated various segregant materials. A study by Shiroyama et al. investigates the use of several metal oxides (MO_x) as segregants and examines the microstructure and magnetic properties of the resultant films [16]. Recently, Xu et al. reported the synthesis of fine, uniform structure films with a boron nitride (BN) segregant [6].

Different substrate materials have also been actively investigated. A study by Sepehri-Amin et al. investigating $MgAl_2O_4$ substrates reports that the choice of the substrate material significantly influences the final magnetic properties of FePt-C films [11]. Studies examining other substrates, including MgTiO/MgTiON [12], CrX (X = Ru, Mo, W, Ti) [18], TiN/RuAl [13], MgON/NiO [15], and $SrTiO_3/MgAl_2O_4/TiO_2$ [14], indicate that the surface energy of the substrate and FePt–substrate lattice mismatch affect the microstructure of FePt nanogranular films.

Besides the identification of new materials for manufacturing FePt thin films, research on process optimization is being actively pursued at present. According to Perumal et al., the amount of C added as a segregant alters the size of FePt grains and the degree of $L1_0$ ordering in FePt [3]. Suzuki et al. report that low-temperature deposition during the initial stage of the sputtering process promotes the nucleation of FePt grains, resulting in films with a fine microstructure [7]. These previous studies indicate a high degree of freedom (in terms of material selection and process optimization) in the synthesis of FePt nanogranular thin films. An accurate understanding of these phenomena is essential for effectively exploring relevant processes and materials.

Experimental studies provide significant insight into microstructure formation in nanogranular FePt films. However, experimental methods are associated with inherent limitations, and relying solely on them could lead to incorrect results. For example, due to the difficulty of in-situ observation, it is experimentally challenging to differentiate between FePt grain coarsening and coalescence. This complicates process optimization for grain refinement. Furthermore, the physical properties of the substrate and segregant (such as lattice constants and surface energy), which are believed to influence microstructure formation [11,12,14,15], cannot be independently varied experimentally. Consequently, despite several attempts [14,15], the individual contributions of these factors toward microstructure formation have not been completely elucidated to date. Another limitation of experimentation is the difficulty in characterizing stress fields. Although elastic strain is believed to play a key role in microstructure formation, the relationship between the stress fields induced within FePt nanogranular films and the resulting microstructure remains unexplained because the direct experimental observation of stress fields is challenging. To overcome these limitations, developing a numerical simulation model capable of reproducing the temporal evolution of the microstructure and associated stress fields during the deposition of FePt-X nanogranular films is vital.

The phase-field (PF) method has emerged as a powerful tool for predicting the complex microstructural evolution of numerous materials [19–23]. This method can simulate a wide range of phenomena that occur during microstructure formation, including spinodal decomposition [23], alloy solidification [20], grain growth in polycrystalline materials [20], and elastic interactions between precipitates [21,22]. Microstructure formation in thin films has been extensively studied using the PF method [24–27]. Yeon et al. first simulated the evolution of a thin-film structure, particularly the adsorption and diffusion of atoms in a sub-monolayer film, using the PF method [27]. Wang et al. simulated the formation of a three-dimensional (3D) island-like structure on a substrate during annealing driven by elastic-strain energy relaxation [25]. Takaki et al. investigated the self-organization of quantum dots during film deposition [24]. Studies on FePt magnetic recording media have also been conducted. Koyama et al. modeled microstructure formation in FePt-X films as the phase separation of FePt and the segregant X [28]. Liu et al. investigated the effect of interfacial energy anisotropy on the microstructure of FePt-X films [29]. Ren et al. evaluated the effect of the misfit strain between FePt and the substrate on microstructure formation [30].

However, previous studies on microstructure formation in FePt-X films model the formation of island-like structures as phase separation occurs through post-deposition annealing. Consequently, these models do not account for microstructural evolution during sputtering. Numerous studies indicate that the microstructure of FePt-X films evolves during sputtering [14]. As sputtering continuously supplies atoms, a model accounting for this continuous influx is necessary to accurately reproduce the microstructural development of FePt-X films. We analyzed FePt-X thin film growth using a phase-field (PF) model that explicitly incorporates the externally supplied atomic flux characteristic of the sputter deposition process. This approach represents the first attempt to physically and realistically reproduce the actual process in which the FePt-X nanogranular microstructure forms during film growth, thereby enabling a more accurate prediction of the temporal evolution of the microstructure. The simulation model, verified by comparison with experimental results, generated results consistent with experiments regarding the morphology and size of the microstructure. Based on the validated model, a series of computational experiments were used to elucidate the mechanisms governing the formation of FePt islands. Furthermore, the relationship between stress fields and microstructure, the role of C as a segregant, and the influence of the sputtering rate on microstructural evolution were investigated. The insights gained from this study provide a clear guideline for material/process design aimed at achieving optimal microstructures in nano-granular films.

2. Methods

2.1. Experimental method

FePt-C films (4.5 nm thick) were synthesized using an ultrahigh-vacuum co-sputtering machine with a base pressure of $\sim 10^{-6}$ Pa. In many studies, FePt-C films are deposited in the temperature range of 400–600 °C to achieve high $L1_0$ ordering and grain density [9,10,12,14,15,17,31]. Following this common practice, all films were deposited on MgO (001) single crystal substrates at 500 °C. The volume fraction of C, which was varied from 25 % to 40 %, was controlled by the deposition rate. A C capping layer (5 nm thick) was deposited at 25 °C.

A Titan G2 80–200 instrument (FEI) with a probe aberration corrector was used for microstructural analysis. Transmission electron microscopy (TEM) samples were manufactured by etching with a mixture of sulfuric and phosphoric acid.

2.2. Calculation model

The PF method [19–22,25] was used to model microstructure formation during the deposition of FePt-C thin films on MgO.

The local volume fraction f_p values of the phase p were used as field variables. Here, $p = 1$, 2, 3, and 4 correspond to vacuum, FePt, C, and MgO respectively. The volume fractions satisfy the condition $\sum_{p=1}^{4} f_p = 1$. Experimental studies on FePt-C films deposited on MgO substrates have shown that the solubility of C in FePt and the interdiffusion of elements between FePt and MgO are negligibly small [12,17]. Therefore, the mutual solubility among the FePt, C, and MgO phases is ignored in the calculation. In this model, FePt is assumed to be ordered into the $L1_0$ structure immediately after deposition; therefore, it is treated as an $L1_0$ structure with the c-axis oriented in the film-thickness direction.

The governing equation for f_p can be expressed as the Cahn–Hilliard equation with an additional convection term, as follows:

$$\frac{\partial f_p}{\partial t} = \nabla \cdot \left(\sum_{q=1}^{4} M_{pq} \nabla \left(\frac{\delta G_{\mathrm{sys}}}{\delta f_q} \right) \right) + B s_p \frac{\partial f_1}{\partial z} \tag{1}$$

Here, M_{pq} is the diffusion mobility, G_{sys} is the total Gibbs energy of the system, B denotes the sputtering rate. The term s_p is the "sputtering composition," which represents the volume ratio of materials supplied to the film surface and corresponds to the final film composition. The

conditions $s_1 = -1$ and $\sum_{p=2}^{4} s_p = 1$ ensure that the vacuum region is replaced by the deposited materials as sputtering progresses. The first term on the right-hand side, representing the diffusion of atoms constituting the film, contributes toward reducing the free energy of the system. The second term represents the supply of atoms by sputtering. The treatment of this term extends the formalism used in PF models for thin-film deposition developed by Takaki et al. [24] to a multi-component system. This formalism considers the process where atoms impinging along the z-direction are supplied to the interface between the vacuum and solid phases. The diffusion mobility M_{pq} can be defined as follows:

$$M = M_0 \begin{pmatrix} 1 & -\frac{1}{2} & -\frac{1}{2} & 0 \\ -\frac{1}{2} & 1 & -\frac{1}{2} & 0 \\ -\frac{1}{2} & -\frac{1}{2} & 1 & 0 \\ 0 & 0 & 0 & 0 \end{pmatrix} \tag{2}$$

where M_0 is a constant that scales the entire diffusion rate. The diffusion mobility M_{pq} is set to 0 when $p = 4$ or $q = 4$ because the MgO substrate is reported to maintain its initial plane throughout the deposition process [8].

The total Gibbs energy can be expressed as follows:

$$G_{sys} = G_{chem} + G_{grad} + G_{str} \tag{3}$$

where G_{chem}, G_{grad}, and G_{str} are the chemical, gradient, and elastic strain energies, respectively. The chemical energy can be expressed as follows:

$$G_{chem} = 2^4 \sum_{p=1}^{4} \sum_{q=p+1}^{4} L_{pq} f_p^2 f_q^2 + 3^6 \sum_{p=1}^{4} \sum_{q=p+1}^{4} \sum_{r=q+1}^{4} L_3 f_p^2 f_q^2 f_r^2 \tag{4}$$

where L_{pq} denotes the height of the barrier potential between the two phases and L_3 is the potential barrier height among the three phases. The gradient energy can be expressed as follows:

$$G_{grad} = -\sum_{p=1}^{4} \sum_{q=p+1}^{4} \kappa_{pq} (\nabla f_p)(\nabla f_q) \tag{5}$$

where κ_{pq} is the gradient energy coefficient.

To reproduce the surface/interface energy γ_{pq} at a two-phase interface with an equilibrium profile, the values of L_{pq} and κ_{pq} are determined using the following equations:

$$L_{pq} = \frac{3\tanh^{-1}(1-2\lambda)}{4 d_{pq}} \gamma_{pq} \tag{6}$$

$$\kappa_{pq} = \frac{3 d_{pq}}{4\tanh^{-1}(1-2\lambda)} \gamma_{pq} \tag{7}$$

where d_{pq} is interface width and λ is the interface cutoff [32].

The elastic strain energy can be expressed as follows:

$$G_{str} = \frac{1}{2} \int_{\boldsymbol{r}} C_{ijkl} (\varepsilon_{ij} - \varepsilon_{ij}^0)(\varepsilon_{kl} - \varepsilon_{kl}^0) d\boldsymbol{r} \tag{8}$$

Here, C_{ijkl} is the elastic constant, ε_{ij} is the total strain, and ε_{ij}^0 is the eigenstrain. The total strain is calculated by solving the mechanical equilibrium equation using the iterative perturbation method [33].

As indicated by Wang et al., a negative C_{ijkl}, causes numerical instability in micromechanical simulations [25]. This is often a problem in calculations involving vacuum regions because areas with negative C_{ijkl} may appear owing to numerical errors. According to Wang et al., this problem can be overcome by introducing interpolation functions that suppress the negative C_{ijkl}. Then, the material density ρ ($\rho_1 = g(f_1 + f_3)$, $\rho_2 = g(f_2)$ and $\rho_3 = g(f_4)$) defined using the interpolation function g, which ensures that negative C_{ijkl} do not occur, was adopted in this study [25].

$$g(f) = \begin{cases} 0 & \text{if } f < 0, \\ f & \text{if } 0 \leqslant f \leqslant 1, \\ 1 & \text{if } 1 < f. \end{cases} \tag{9}$$

Using the material density, the elastic constant can be expressed as follows:

$$C_{ijkl} = \sum_{p=1}^{3} C_{ijkl}^p \rho_p \tag{9}$$

where C_{ijkl}^p is the elastic constant of phase p. The literature values of the elastic constants of $L1_0$-FePt and MgO were used in this study [34–40]. The elastic constant for vacuum was set to zero. Since C is deposited as an amorphous phase in FePt-C thin films [41,42], it is incoherent with surrounding crystal phases and with itself. Therefore, the amorphous C phase is expected to interrupt stress transfer across different atomic layers by disrupting lattice continuity [43]. To reproduce this physical role of C within our model, its elastic modulus was set to zero. It should be noted that this numerical treatment represents the stress relaxation caused by lattice incoherency and does not assume that the actual elastic constant of amorphous C is zero. Consequently, C was treated by the same material density as vacuum ($\rho_1 = g(f_1 + f_3)$) to avoid a negative C_{ijkl}.

The eigenstrain ε_{kl}^0 can be expressed as follows:

$$\varepsilon_{ij}^0 = \sum_{p=1}^{3} \varepsilon_0^{(p)} \rho_p \tag{10}$$

$$\varepsilon_0^{(1)} = \varepsilon_0^{(2)} = \alpha \begin{pmatrix} \eta_a & 0 & 0 \\ 0 & \eta_a & 0 \\ 0 & 0 & \eta_c \end{pmatrix} \tag{11}$$

$$\varepsilon_0^{(3)} = \begin{pmatrix} 0 & 0 & 0 \\ 0 & 0 & 0 \\ 0 & 0 & 0 \end{pmatrix} \tag{12}$$

$$\eta_a = \frac{a_{FePt} - a_{MgO}}{a_{MgO}} \tag{13}$$

$$\eta_c = \frac{c_{FePt} - a_{MgO}}{a_{MgO}} \tag{14}$$

where we introduced the parameter α to control the magnitude of lattice misfit. a_{FePt}, c_{FePt}, and a_{MgO} are the lattice constants of $L1_0$-FePt (those with an FePt subscript) and MgO (those with an MgO subscript). During FePt deposition on MgO, misfit dislocations are introduced at the FePt/MgO interface, relaxing the strain due to lattice misfit [11,12,14]. To reproduce this effect, the misfit was effectively reduced using the coefficient α ($0 \leqslant \alpha \leqslant 1$).

2.3. Calculation conditions

A plan view of the initial FePt nucleus microstructure is shown in Fig. 1 (a). The red, green, and blue regions represent the phases: $L1_0$-FePt, MgO, and C, respectively. In the initial stage of FePt film sputtering, fine FePt grains were uniformly dispersed on the MgO substrate [7]. Therefore, randomly dispersed FePt nuclei of the minimum size that are not unstable were used as the initial film. To generate the initial film microstructure, a two-dimensional phase-separation simulation of the FePt-70 % C film was conducted using the first term on the right-hand side of Eq. (1). A 1.0 nm-thick initial film placed on a 21 nm-thick MgO substrate was used as the initial field for subsequent simulations (Fig. 1 (b)). Notably, the individual thicknesses of the FePt and C phases

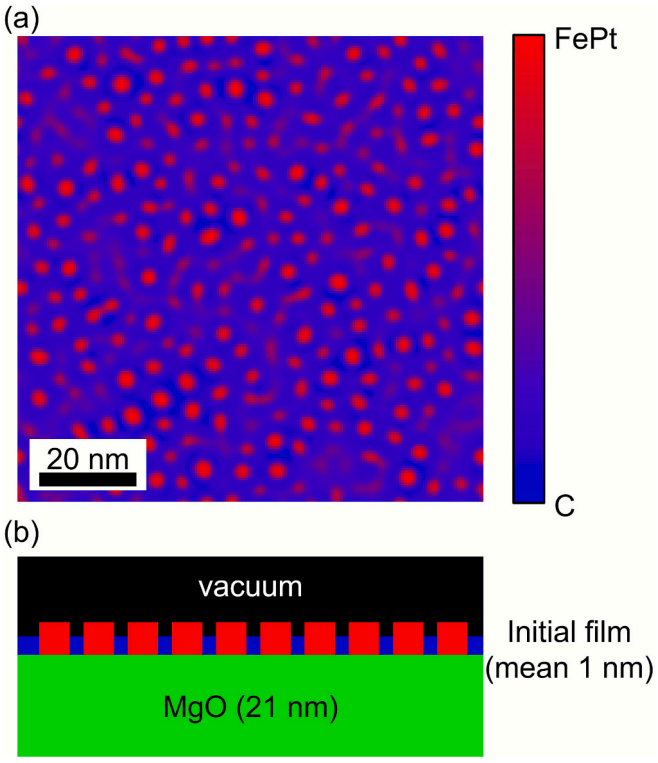

Fig. 1. Microstructure of the initial film (a), and schematics of the initial field used in simulations (b).

were adjusted independently to match the initial film composition to the sputtering composition s_p while maintaining a mean film thickness of 1 nm. Table 1 lists the parameters used in this study. The values of the lattice constant a_p, elastic constant C_{ij}^p, and surface energy of FePt $\gamma_{\text{FePt-vac}}$ and MgO $\gamma_{\text{MgO-vac}}$ were adopted from the literature [34–39]. In the literature, the surface energy of C $\gamma_{\text{C-vac}}$ is a very small value (0.046 Jm^{-2}) [40], which induces numerical instability during the simulations. To avoid this issue, a relatively large value, calculated as 1/10 of $\gamma_{\text{FePt-vac}}$, was used in simulations. Values for the diffusion mobility M_0, misfit parameter α, and interfacial energy γ_{pq} were not found in the literature. Therefore, these parameters were adjusted to quantitatively reproduce the experimental microstructures. In addition, periodic and zero Neumann boundary conditions were employed in the in-plane and out-of-plane directions of the film, respectively, during simulations.

Table 1
Parameters used in simulations.

Simulation area (nm)	$96 \times 96 \times 32$	–
Computational cell dimensions	$192 \times 192 \times 64$	–
Mobility, $M_0/\text{m}^5\text{s}^{-1}\text{J}^{-1}$	3.37×10^{-29}	–
Sputtering rate, B/nm s^{-1}	1.60×10^{-2}	–
Surface energy, $\gamma_{p\text{-vac}}/\text{Jm}^{-2}$	$\gamma_{\text{FePt-vac}} = 2.10$, $\gamma_{\text{C-vac}} = 0.21$, $\gamma_{\text{MgO-vac}} = 1.16$	[36,39]
Interface energy, $\gamma_{p\text{-}q}/\text{Jm}^{-2}$	$\gamma_{\text{FePt-C}} = 2.10$, $\gamma_{\text{FePt-MgO}} = 0.58$, $\gamma_{\text{C-MgO}} = 1.16$	–
Potential barrier, L_3/Jm^{-3}	1.73×10^9	–
Interface cutoff, λ	0.1	[32]
Interface width, d_{pq}/nm	1.5	–
Lattice constants, a_p, c_p/nm	$a_{\text{FePt}} = 0.3849$, $c_{\text{FePt}} = 0.3700$, $a_{\text{MgO}} = 0.4212$	[34,35]
Elastic constants, C_{ij}^p/GPa	$C_{11}^{\text{FePt}} = 261$, $C_{33}^{\text{FePt}} = 299$, $C_{12}^{\text{FePt}} = 169$, $C_{13}^{\text{FePt}} = 151$, $C_{44}^{\text{FePt}} = 103$, $C_{66}^{\text{FePt}} = 133$, $C_{11}^{\text{MgO}} = 297.8$, $C_{12}^{\text{MgO}} = 97.0$, $C_{44}^{\text{MgO}} = 156.3$	[37,38]
Misfit coefficient, α	0.7	–

3. Results

The temporal evolution of the film microstructure during the sputtering of FePt-35 %C is shown in Fig. 2. The 3D view, plan view on the [001] direction, and cross-sectional view of the (010) plane along with the mean film thickness at each point of time are demonstrated. With progress in sputtering, the film thickness increases with increasing supply of atoms onto the film surface. Consequently, the FePt grains increase in size through both growth and coalescence, ultimately forming an island-like structure. A TEM micrograph of the experimentally fabricated 4.5 nm-thick FePt-35 %C film is shown in Fig. 3. Both calculations and experimental results indicate a well-separated island-like structure of FePt grains in this film. Interestingly, the simulation results reproduce the experimentally observed rounded squareness of the FePt grains and their periodic arrangement along the [100] and [010] direction. According to the literature, elastic anisotropy influences the in-plane anisotropy of thin-film microstructures [26], while surface-energy anisotropy affects FePt-C nanogranular films [31]. As the PF model used in this study assumes isotropic surface and interfacial energies, the anisotropy observed in the simulations can be attributed to the elastic anisotropies of MgO and FePt. It is noted that this result does not deny the contribution of surface energy anisotropy to the morphological anisotropy in actual microstructures. During the time evolution of the thin-film microstructure, the FePt grains grow in size owing to coarsening and coalescence with progress in sputtering (Fig. 2(a–d)). Simulations and experiment indicate a final average grain diameter of 12.4 nm and 9.2 nm, respectively. While our results successfully reproduce the characteristic microstructures, there are slight quantitative discrepancies in grain size. These differences can be attributed to simplifications in the simulation model. For simplicity and to keep computational costs reasonable, we did not consider factors such as surface energy anisotropy and surface diffusion, which are thought to influence microstructure formation. These omitted factors could be responsible for the observed discrepancy. Moreover, simulations indicate that adjacent FePt grains are connected as they grow, forming irregular L- or U-shaped grains, consistent with experimental observations (Fig. 3) and the literature [7–10,15,17,31]. Thus, according to simulations, the coalescence of multiple FePt grains is the main factor affecting the formation of irregularly shaped grains that are unfavorable for magnetic recording.

In addition, simulations show that the height of the FePt grains at the end of sputtering is greater than that of the C segregant, indicating the preferential growth of FePt grains in the vertical direction (Fig. 2(d)). This phenomenon, the cause for which is discussed in Section 4.2, is expected to contribute toward the formation of island-like structures by suppressing growth in the lateral direction.

The stress field calculated inside the film of Fig. 2 (d) is represented as Fig. 4. The stress-field cross section lies on the (010) plane, and the stress acting along the [100] direction on the (100) plane (σ_{11}) is shown in this figure. The tensile and compressive stresses are marked in red and blue, respectively. Because of the diffused interface treatment in the PF model [44], the local volume fraction of each phase changes continuously across the interface, resulting in a slight penetration of the calculated stress values at the interface region. The stress observed in the C and vacuum regions is a calculation artifact. The in-plane lattice constant of FePt ($a_{\text{FePt}} = 0.3849$ nm) is smaller than that of MgO ($a_{\text{MgO}} = 0.4212$ nm); consequently, tensile stress develops in the FePt grains. A lattice mismatch between FePt and MgO ($\eta_a = -8.7$ %; considered as -6.1 % in calculations after multiplication with the misfit strain coefficient α) leads to large peak stresses (>10 GPa) within the FePt grain. Compressive stress occurs in MgO in contact with FePt, while tensile stress arises on the surface of MgO that is not in contact with FePt, likely because the compression of the MgO lattice in contact with FePt causes the adjacent MgO lattice to experience tensile strain. Stress analysis within the FePt grains indicates that the tensile stress decreases with increasing distance from the MgO substrate, likely because the stress,

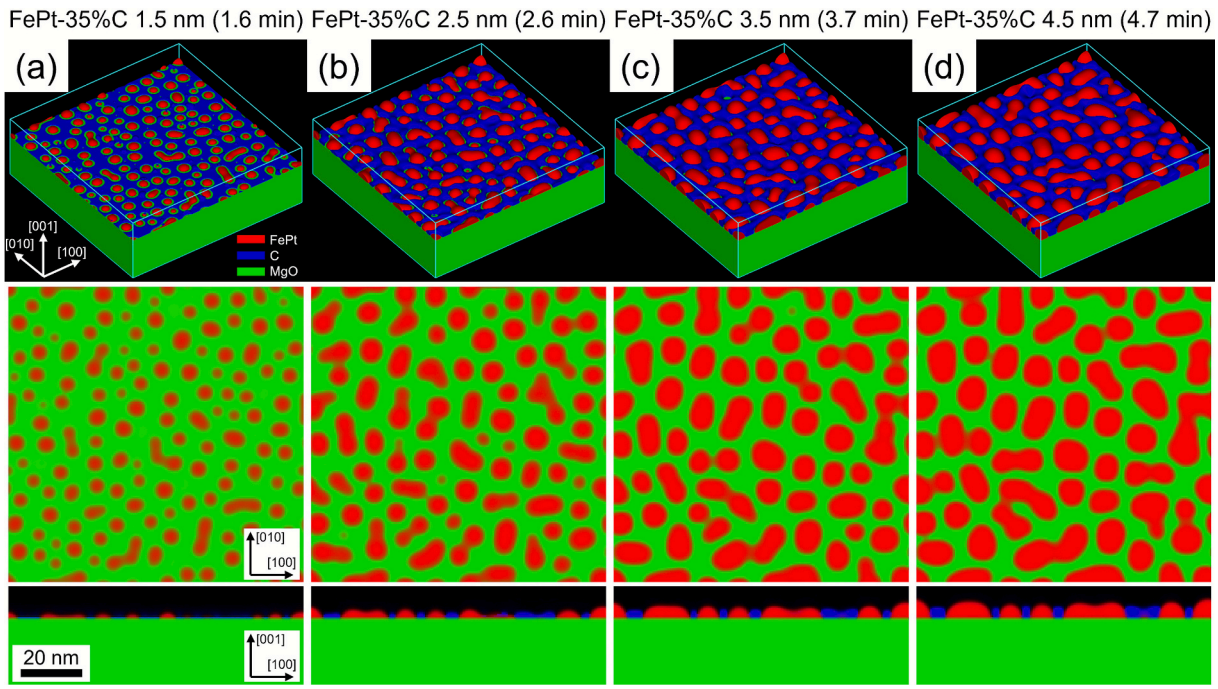

Fig. 2. Simulation results of the microstructure evolution of FePt-35 %C films with a thickness of (a) 1.5, (b) 2.5, (c) 3.5, and (d) 4.5 nm. The 3D, in-plane projection, and cross-sectional views are shown. The red, green, and blue regions represent $L1_0$-FePt, MgO, and C, respectively. C is not shown in the in-plane projection for clarity. (For interpretation of the references to colour in this figure legend, the reader is referred to the web version of this article.)

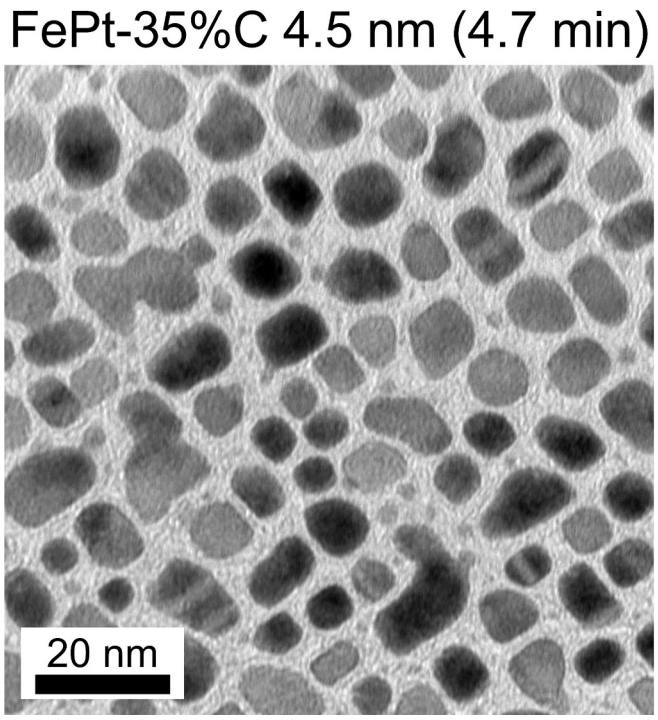

Fig. 3. TEM micrography of a 4.5 nm-thick FePt-35 % C film deposited on an MgO substrate at 500 °C.

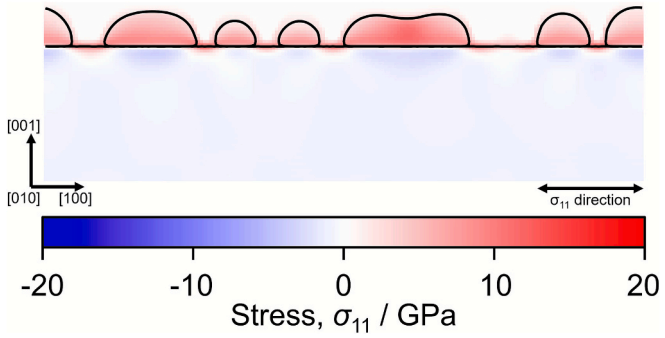

Fig. 4. The (010) cross-sectional view of the calculated stress field (σ_{11}) for a FePt-35%C film. The contours of FePt and MgO are superimposed. Positive and negative values represent tensile and compressive stress, respectively.

which originates from the lattice mismatch between FePt and MgO, diminishes with increasing distance from the interface between these phases. The tensile stress within FePt grains is considered the primary driving force for $L1_0$ ordering and its variant selection [18]. Therefore, these results indicate a tradeoff: a high aspect ratio (h/D), which is necessary for a high magnetic recording density, may prevent high degrees of $L1_0$-ordering, which is also critical for a high magnetic recording density. Notably, in this study, the horizontally extended grains exhibit high internal tensile stress, consistent with the predictions of analytical studies [45] and simulations [25].

The microstructures of 4.5 nm-thick FePt-x%C films with C contents of $x = 40$ %, 30 %, and 25 % are compared in Fig. 5. The TEM results of experimentally fabricated films with the same compositions and thicknesses are shown in Fig. 6. In both simulations and experiments, the sputtering rates were set to the FePt deposition rate used for the FePt-35 %C film (Fig. 2). Consequently, films with a higher C content were deposited within a shorter time. Both simulations and experiments indicate a reduction in the FePt grain size with increasing C content. This aligns with previous reports [3,17] and confirms the ability of the simulation to accurately reproduce the experimentally observed effect of the C content in the films. Furthermore, films with a lower C content exhibit a greater degree of grain coalescence, resulting in an increased prevalence of grains with an irregular shape and high in-plane aspect ratios. Collectively, these findings suggest that the PF model developed in this study effectively simulates the essential features of microstructural evolution during the sputtering of FePt-C thin films.

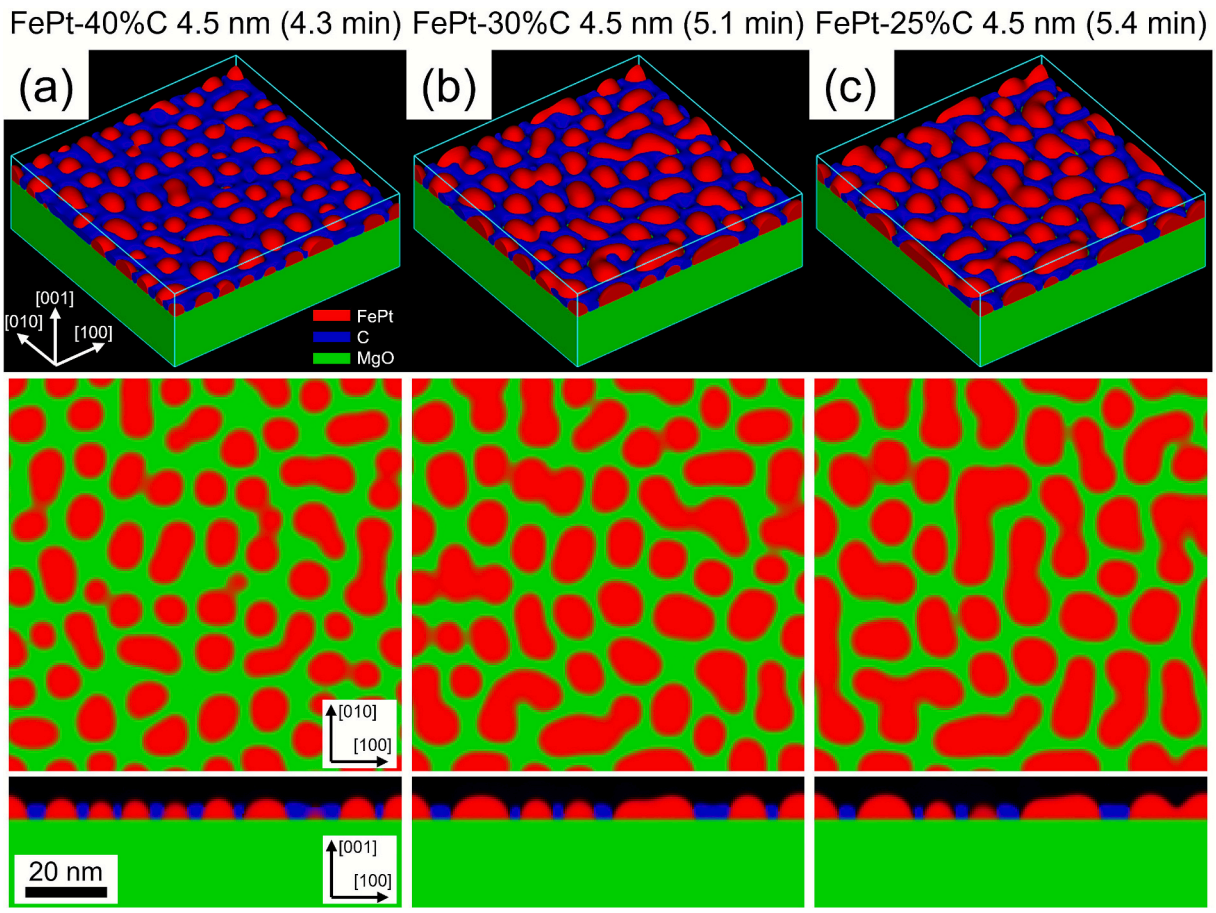

Fig. 5. Simulated microstructure of (a) FePt-40%C, (b) FePt-30%C, and FePt-25%C films. The 3D, in-plane projection, and cross-sectional views are shown. The red, green, and blue regions represents $L1_0$-FePt, MgO, and C, respectively. C is not shown in the in-plane projection for clarity. (For interpretation of the references to colour in this figure legend, the reader is referred to the web version of this article.)

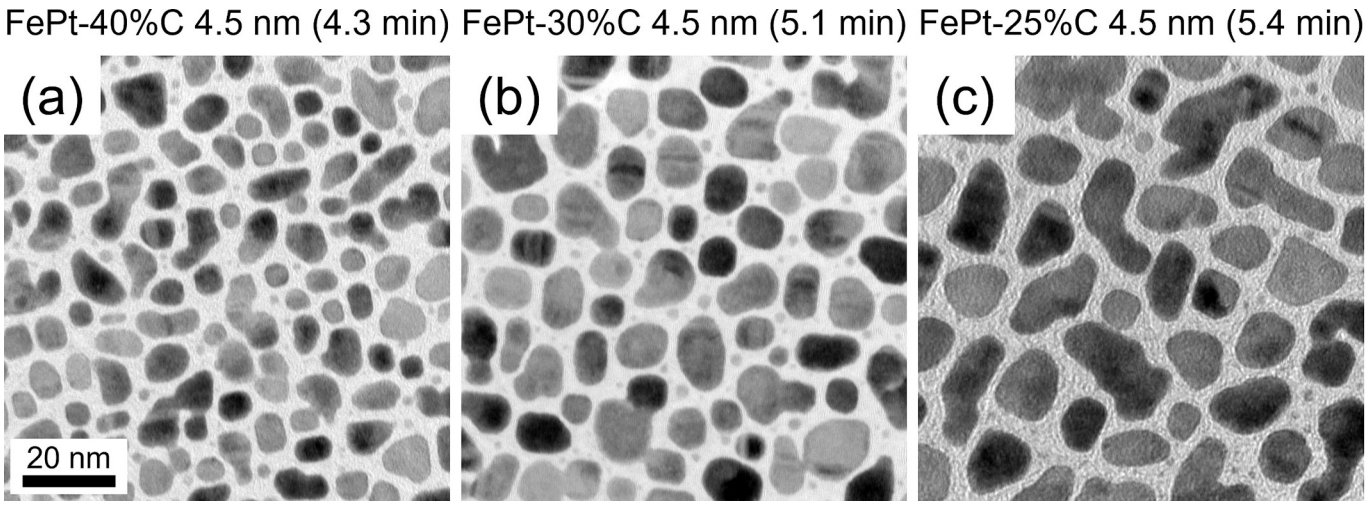

Fig. 6. BF-TEM images of 4.5 nm-thick (a) FePt-40 %C, (b) FePt-30 %C, and (c) FePt-25 %C films deposited on an MgO substrate at 500 ℃.

4. Discussion

Microstructure formation in FePt-C nanogranular films is a complex phenomenon influenced by numerous factors, such as the lattice constant and surface energy of the substrate [11,12,14,15]. Many of these conditions, which depend on material properties, are difficult to change independently in experiment. In the previous section, the simulation and experimental results for four FePt-C films are described, and the proposed simulation model is validated by comparing the simulated and experimental film microstructures. In this section, the validated model is used to discuss the influence of several factors, namely, elastic strain, segregant addition, and sputtering rate, on the formation of island-like structures in FePt films.

4.1. Influence of elastic strain energy

Calculations setting the misfit parameter α in Eq. (11) to 0, effectively ignoring the elastic strain energy, were used to investigate the influence of the elastic strain energy resulting from lattice mismatch between the substrate and FePt. Since the model considers only elastic and surface/interface energies, microstructure evolution is driven solely by the surface/interface energy under these conditions. The temporal evolution of the microstructure of FePt-35 %C obtained from this simulation (Fig. 7) indicates the formation of a coarse network-like structure in which adjacent FePt grains are connected; this behavior differs from that observed when the elastic strain energy is considered (Fig. 2). These results suggest that elastic strain energy contributes to the formation of a uniform, fine island-like microstructure, while surface/interface energy drives coarsening.

Schematics of the stress induced in a FePt-C nanogranular film deposited on MgO are illustrated in Fig. 8. As shown in Fig. 4, the stress generated within the FePt grains decreases with increasing distance from the FePt/MgO interface. This allows FePt to effectively relieve elastic strain energy by prioritizing vertical growth. This phenomenon is confirmed by the observation that the grains extending horizontally in Fig. 4 experience significant tensile stress. Therefore, from an energetic perspective, vertically elongated structures are more stable because lower stresses correspond to lower elastic strain energy.

Importantly, the MgO-substrate surface that is not in contact with FePt experiences tensile stress (Fig. 4). In these regions, the MgO lattice expands owing to elastic strain, increasing the lattice mismatch with FePt. As a consequence, the formation of a new FePt/MgO interface in these regions is associated with a significant increase in elastic energy; thus, such interface is unlikely to form. This effect is expected to suppress the coalescence of adjacent FePt grains, contributing toward the formation of a fine and uniform island-like microstructure.

In summary, the elastic strain energy simultaneously promotes the preferential vertical growth of FePt grains and inhibits their coalescence, likely contributing toward the formation of an island-like microstructure, which is crucial for a high magnetic recording density. This mechanism resembles the Volmer–Weber growth mode of single-phase films [46]. Although FePt-C films are multiphase, the absence of elastic influence from amorphous C enables the system to exhibit a growth mechanism similar to that of single-phase films.

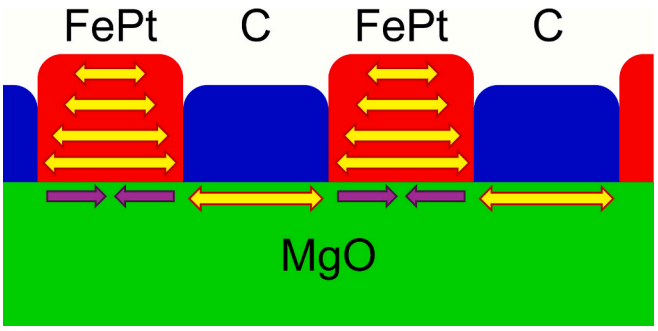

Fig. 8. Schematics of stress generation caused by lattice misfit between FePt and MgO in the island-like film microstructure. Yellow and purple arrows indicate tensile and compressive stress, respectively. (For interpretation of the references to colour in this figure legend, the reader is referred to the web version of this article.)

4.2. Influence of C addition

The addition of C as a segregant to refine FePt grain size represents a significant breakthrough in the development of FePt-based magnetic recording media [3]. This section discusses details of the effects of C addition on the microstructure formation. Simulations indicating the

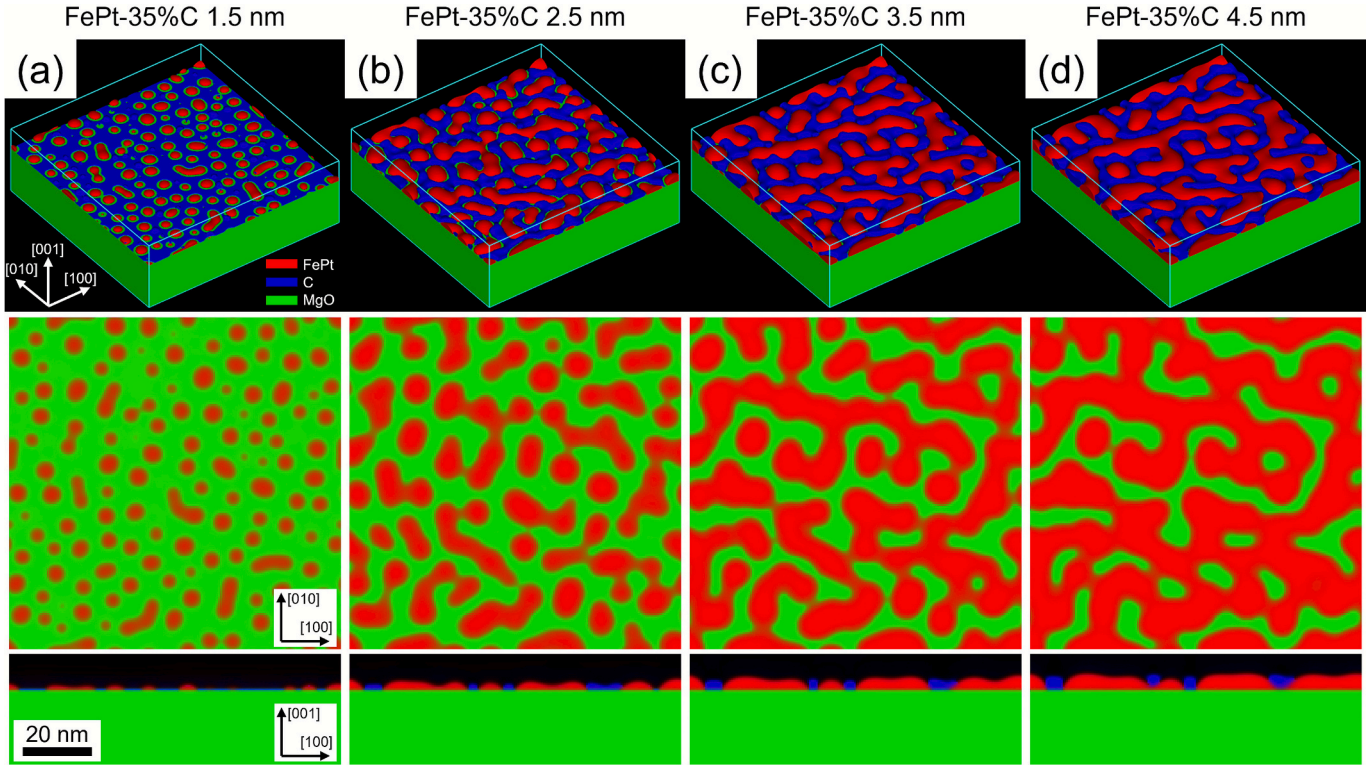

Fig. 7. Simulation results of the microstructure evolution of FePt-35 %C films with a thickness of (a) 1.5, (b) 2.5, (c) 3.5, and (d) 4.5 nm when elastic strain energy is not considered. The 3D, in-plane projection, and cross-sectional views are shown. The red, green, and blue regions represents $L1_0$-FePt, MgO, and C, respectively. C is not shown in the in-plane projection for clarity. (For interpretation of the references to colour in this figure legend, the reader is referred to the web version of this article.)

temporal evolution of the microstructure of a film without the C segregant are shown in Fig. 9. In these simulations, the amount of sputtered FePt and the deposition rate of FePt were set to be the same as those used for the FePt-35 %C film (Fig. 2). In the early stages of deposition (Fig. 9 (a–c)), island-like structures are formed, consistent with the simulation results with C addition shown in Fig. 2. However, the final microstructure (Fig. 9 (d)) differs from that simulated with C addition (Fig. 2 (d)). The average FePt grain size in the absence of C is significantly larger than that with C addition. Moreover, a large portion of FePt grains shows an elongated and irregular shape without C addition. A comparison of Fig. 9 (c) and (d) indicates that these grains are formed by the coalescence of adjacent grains. These results suggest that the addition of C suppresses FePt grain coalescence and refines the grain size. Thus, in addition to the relaxation of the elastic strain energy, the C segregant plays an important role in suppressing the coalescence of FePt grains and promoting the formation of well-separated, uniform island-like structures.

The PF model evolves systems to minimize their total Gibbs energy. The observed effects of C addition can be attributed to changes in the surface, interface, and elastic energies induced by C segregation. However, these energy changes are unlikely to significantly affect microstructure formation in our simulations. As listed in Table 1, the interfacial energies between FePt and C and between MgO and C are set equal to their respective surface energies ($\gamma_{\text{FePt-vac}} = \gamma_{\text{FePt-C}}$, $\gamma_{\text{MgO-vac}} = \gamma_{\text{C-MgO}}$) in the simulations, and the surface energy of C ($\gamma_{\text{C-vac}} = 0.21\ \text{Jm}^{-2}$) is significantly lower than those of the other phases. Moreover, as outlined in the Computational Methods section, C and vacuum are treated equivalently in elastic-strain energy calculations; i.e., C is considered energetically equivalent to vacuum in the proposed model. Therefore, the observed differences in microstructure arising from the presence or absence of C grain boundaries are unlikely to be attributable to modifications in the surface or elastic strain energy.

A plausible explanation for the effect of C addition is that C alters the diffusion paths of Fe and Pt atoms in the system (schematics are shown in Fig. 10). In the absence of C, FePt atoms deposited via sputtering are

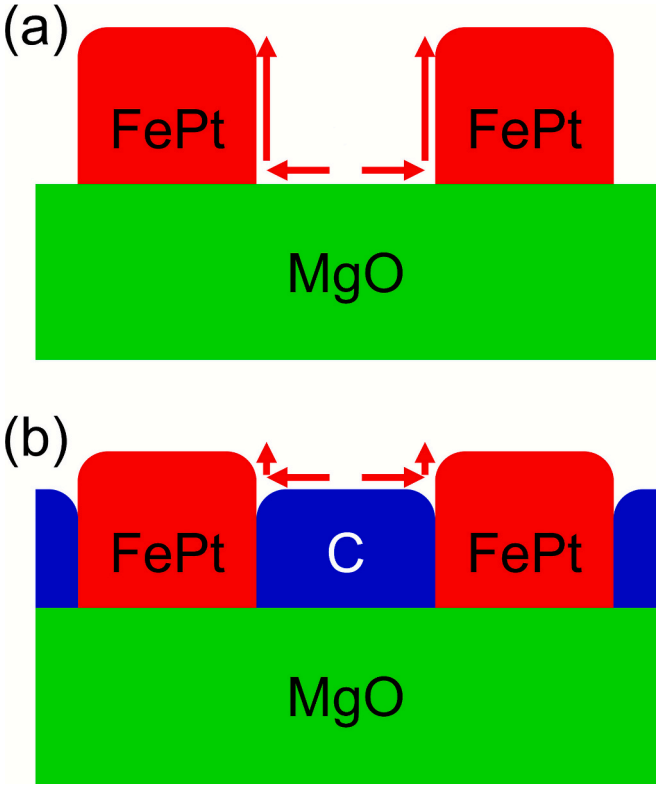

Fig. 10. Schematics of diffusion-path changes caused by segregant addition.

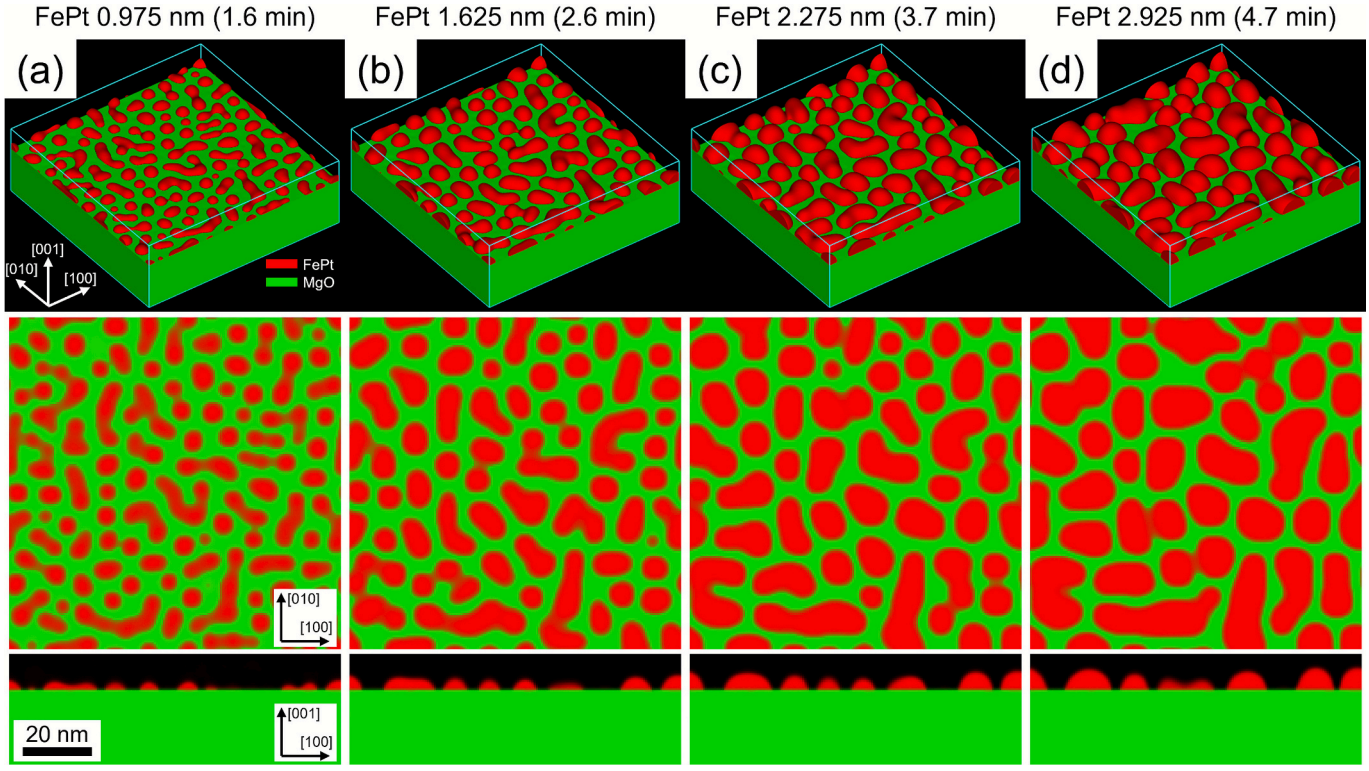

Fig. 9. Simulation results for the microstructure evolution of a film without segregant addition with a thickness of (a) 0.975, (b) 1.625, (c) 2.275, and (d) 2.925 nm. The 3D, in-plane projection, and cross-sectional views are shown. The red and green regions represent $L1_0$-FePt and MgO, respectively. (For interpretation of the references to colour in this figure legend, the reader is referred to the web version of this article.)

supplied to either the existing FePt grains or the MgO substrate. For the vertical growth of FePt, the atoms supplied to the MgO substrate must diffuse over a long distance, as shown in Fig. 10 (a). In contrast, on C addition, Fe and Pt atoms are supplied to the C surface rather than the MgO substrate. This shortens the diffusion distance required for vertical growth, as shown in Fig. 10 (b), promoting vertically oriented growth.

This mechanism is applicable to the system, regardless of the type of material used as the segregant. However, previous studies indicate that the choice of the segregant material affects the FePt microstructure significantly [3,4,6,12,16,17]. For example, according to Shiroyama et al., using the metal oxide MO_x (M=Nb, W, Zr, Al) as a segregant can lead to the formation of network-like structures, deteriorating the magnetic properties of the system. Possible reasons for this phenomenon include changes in the lattice constant of FePt due to segregant-element dissolution and a significant change in the surface/interface energy balance. Systematic investigation of these factors, critical for segregant material selection, will be key in future research.

4.3. Impact of sputtering rate

The governing equation (Eq. (1)) includes diffusion and sputtering terms. The formation of an island-like microstructure occurs through competition between the supply of atoms by sputtering and the transport of these atoms by diffusion. Therefore, the relative rates of diffusion and sputtering are expected to affect the final film microstructure. To investigate this effect, microstructures derived from calculations with different values of the sputtering rate B were compared. The simulation results obtained by altering B from the baseline value listed in Table 1 ($B = 1.60 \times 10^{-2}$ nm s^{-1}) to 1.00×10^{-2} and 3.20×10^{-2} nm s^{-1} are shown in Fig. 11 (a) and (c); for comparison, the simulation results obtained with the baseline value are shown in Fig. 11. In these calculations, the final film thickness and composition are set to the same values as those used for the results shown in Fig. 2. A comparison of Fig. 11 (a) with Fig. 11 (b) indicates that a reduction in the sputtering rate from 1.60×10^{-2} nm s^{-1} to 1.00×10^{-2} nm s^{-1} results in a reduction in grain density from 5100 to 4991 μm^{-2}. This can be attributed to grain coarsening owing to Ostwald ripening [47], which is facilitated by the extended deposition time. Conversely, an increased sputtering rate induces significant grain coalescence, resulting in a network-like structure (Fig. 11 (c)). This can be attributed to the insufficient diffusion time available for the formation of energetically stable island-like structures. During the sputtering of FePt-C films, atoms are supplied to the upper surfaces of the existing FePt grains and the C segregant. Driven by Gibbs energy minimization (as described in the first term in Eq. (1)), the supplied Fe, Pt, and C atoms undergo diffusion. As previously discussed, island-like structures are energetically favorable for relieving elastic strain; thus, an island-like structure forms when sufficient diffusion time is available. However, with limited diffusion time, a more energetically unstable fine network-like structure that requires less diffusion time for formation develops. Previous studies report the formation of similar network-like structures on low-temperature sputtering [7]; this can be attributed to slow diffusion at low temperatures, which prolongs the time required to form energetically stable island-like structures, resulting in the observed network morphology.

These findings suggest that an optimal sputtering rate exists for the production of uniform fine-grained FePt. Sputtering at a high rate that

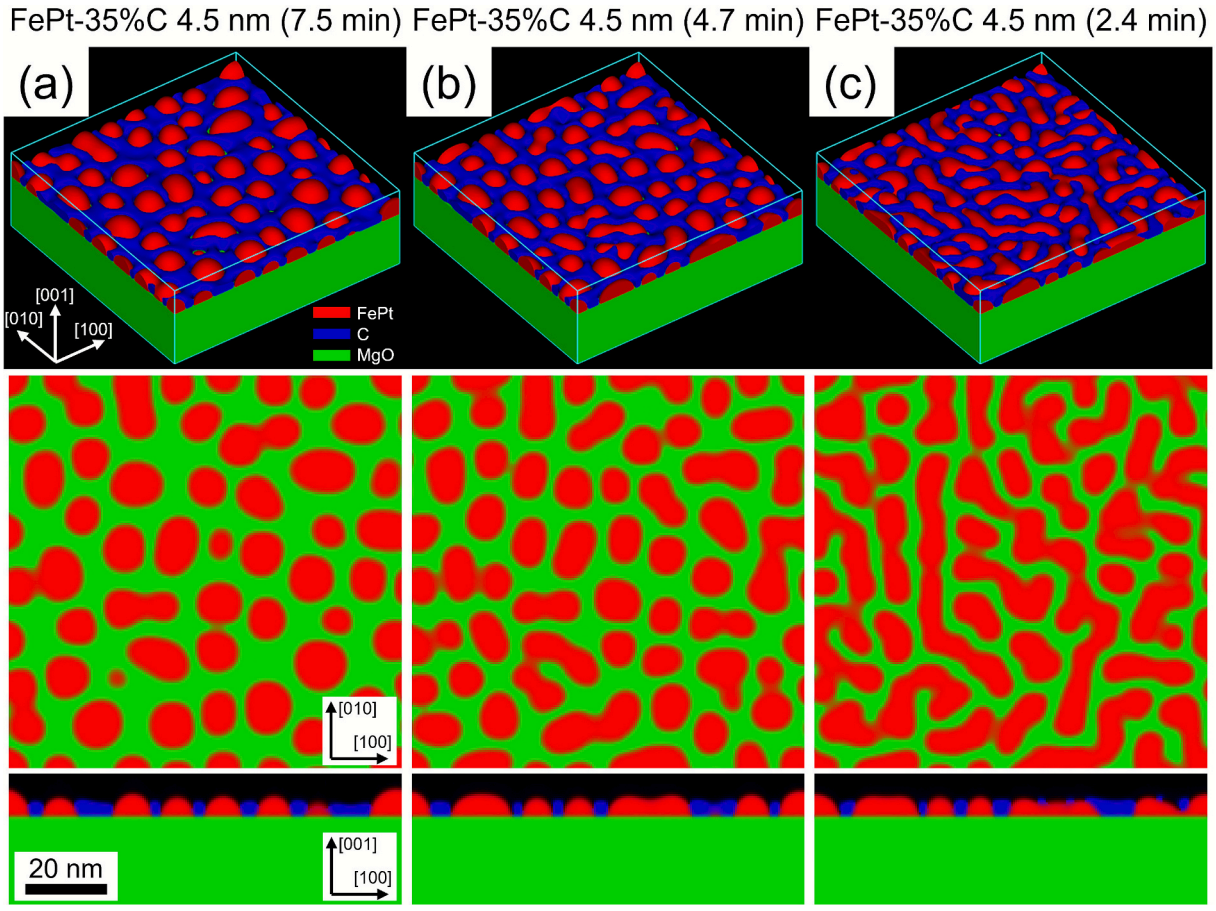

Fig. 11. Simulation results for the microstructure evolution of a FePt-35 %C film with a sputtering rate of (a) 1.00×10^{-2}, (b) 1.60×10^{-2}, and (c) 3.20×10^{-2} nms^{-1}. The 3D, in-plane projection, and cross-sectional views are shown. The red, green, and blue regions represent $L1_0$-FePt, MgO, and C, respectively. C is not shown in the in-plane projection for clarity. (For interpretation of the references to colour in this figure legend, the reader is referred to the web version of this article.)

does not cause significant grain coalescence will be effective for fabricating fine FePt grains. Due to the temperature-dependent diffusion rate, the optimal rate increases with higher sputtering temperatures. These results emphasize that both energetic and kinetic factors are important for the formation of fine island-like structures in FePt films.

5. Conclusion

Microstructure formation in FePt-C nanogranular films on MgO substrates during sputtering was modeled using the PF method in this study. Calculations were used to elucidate the factors necessary for forming well-isolated microstructures that are essential for high recording densities. The conclusions of this study can be summarized as follows:

- PF simulations accurately reproduced the experimentally observed microstructures of FePt-C films with different amounts of C addition.
- Calculations indicated that the relaxation of the elastic strain energy plays a key role in the formation of island-like microstructures.
- The addition of C as a segregant modifies the diffusion paths of the atoms supplied during sputtering, contributing toward the formation of an island-like structure by promoting the vertical growth of FePt grains.
- Increasing the sputtering rate relative to the diffusion rate results in microstructural refinement; however, excessively high sputtering rates can induce significant grain coalescence.

The results of this study provide insights into optimizing the conditions for synthesizing high-performance FePt magnetic recording films. Based on the findings, the following material selection and process design guidelines were derived:

- Select a substrate material with the maximum lattice mismatch that allows epitaxial growth.
- Use a segregant materials that do not exhibit coherence with the substrate and FePt.
- Perform sputtering at the highest sputtering rate that does not cause significant grain coalescence.

These guidelines are expected to contribute significantly to future developments in magnetic recording media by enabling systematic optimization of materials and processes.

CRediT authorship contribution statement

Yusuke Matsuoka: Writing – original draft, Visualization, Methodology, Investigation, Data curation, Conceptualization. **Machiko Ode:** Writing – review & editing, Supervision, Methodology. **Taichi Abe:** Writing – review & editing, Supervision, Methodology. **Toshiyuki Koyama:** Writing – review & editing, Supervision, Methodology. **Yukiko K. Takahashi:** Writing – review & editing, Project administration, Methodology, Investigation, Funding acquisition, Data curation.

Declaration of competing interest

The authors declare that they have no known competing financial interests or personal relationships that could have appeared to influence the work reported in this paper.

Acknowledgments

This work was supported by JST, CREST Grant Number JPMJCR22C3, and the MEXT Program: Data Creation and Utilization-Type Material Research and Development Project Grant Number JPMXP1122715503.

Data availability

Data will be made available on request.

References

[1] IEA, Energy and AI, Paris, 2025. https://www.iea.org/reports/energy-and-ai.
[2] D. Weller, G. Parker, O. Mosendz, E. Champion, B. Stipe, X. Wang, T. Klemmer, G. Ju, A. Ajan, A HAMR Media Technology Roadmap to an Areal Density of 4 Tb/in2, IEEE Trans. Magn. 50 (2014) 3100108, https://doi.org/10.1109/TMAG.2013.2281027.
[3] A. Perumal, Y.K. Takahashi, K. Hono, FePt-C nanogranular films for perpendicular magnetic recording, J. Appl. Phys. 105 (2009), https://doi.org/10.1063/1.3075986.
[4] M. Watanabe, T. Masumoto, D.H. Ping, K. Hono, Microstructure and magnetic properties of FePt–Al–O granular thin films, Appl. Phys. Lett. 76 (2000) 3971–3973, https://doi.org/10.1063/1.126838.
[5] K. Hono, Y.K. Takahashi, G. Ju, J.U. Thiele, A. Ajan, X.M. Yang, R. Ruiz, L. Wan, Heat-assisted magnetic recording media materials, MRS Bull. 43 (2018) 93–99, https://doi.org/10.1557/mrs.2018.5.
[6] C. Xu, B.S.D.C.S. Varaprasad, D.E. Laughlin, J.G. Zhu, Bias sputtering of granular L10-FePt films with hexagonal boron nitride grain boundaries, Sci. Rep. 13 (2023) 1–10, https://doi.org/10.1038/s41598-023-38106-9.
[7] I. Suzuki, J. Wang, Y.K. Takahashi, K. Hono, Control of grain density in FePt-C granular thin films during initial growth, J. Magn. Magn. Mater. 500 (2020) 166418, https://doi.org/10.1016/j.jmmm.2020.166418.
[8] T. Shiroyama, B.S.D.C.S. Varaprasad, Y.K. Takahashi, K. Hono, Influence of MgO underlayers on the structure and magnetic properties of FePt-C nanogranular films for heat-assisted magnetic recording media, AIP Adv. 6 (2016) 10, https://doi.org/10.1063/1.4964930.
[9] J. Wang, D. Liu, I. Suzuki, Y. Takahashi, M. Yan, K. Hono, High melting point metal (Pt, W) seed layer for grain size refinement of FePt-based heat-assisted magnetic recording media, Appl. Phys Express 12 (2019) 4, https://doi.org/10.7567/1882-0786/aafca3.
[10] J. Wang, H. Sepehri-Amin, Y.K. Takahashi, T. Ohkubo, K. Hono, Magnetic in-plane components of FePt nanogranular film on polycrystalline MgO underlayer for heat-assisted magnetic recording media, Acta Mater. 177 (2019) 1–8, https://doi.org/10.1016/j.actamat.2019.07.017.
[11] H. Sepehri-Amin, H. Iwama, T. Ohkubo, T. Shima, K. Hono, Microstructure and in-plane component of L10-FePt films deposited on MgO and MgAl2O4 substrates, Scr. Mater. 130 (2017) 247–251, https://doi.org/10.1016/j.scriptamat.2016.12.018.
[12] H. Sepehri-Amin, M. Nagano, T. Seki, H. Ho, D. Tripathy, S. Pirzada, K. Srinivasan, H. Yuan, P. Dorsey, A. Ajan, K. Hono, Microstructure and magnetic properties of FePt-(C,SiO2) granular films deposited on MgO, MgTiO, and MgTiON underlayers, Scr. Mater. 157 (2018) 1–5, https://doi.org/10.1016/j.scriptamat.2018.07.025.
[13] E. Yang, S. Ratanaphan, J.G. Zhu, D.E. Laughlin, Structure and magnetic properties of L10-FePt thin films on TiN/RuAl underlayers, J. Appl. Phys. 109 (2011) 7–10, https://doi.org/10.1063/1.3565418.
[14] I. Suzuki, H. Sepehri-Amin, K. Hono, Y.K. Takahashi, Control of grain density by varying lattice mismatch in FePt-C film for heat assisted magnetic recording, J. Alloys Compd. 968 (2023) 172196, https://doi.org/10.1016/j.jallcom.2023.172196.
[15] I. Suzuki, S. Kubo, H. Sepehri-Amin, Y.K. Takahashi, Dependence of the Growth Mode in Epitaxial FePt Films on Surface Free Energy, ACS Appl. Mater. Interfaces 13 (2021) 16620–16627, https://doi.org/10.1021/acsami.0c22510.
[16] T. Shiroyama, T. Abe, Y. Takahashi, K. Hono, Microstructure and magnetic properties of FePt-MOx granular films, IEEE Trans. Magn. 49 (2013) 3616–3619, https://doi.org/10.1109/TMAG.2013.2239963.
[17] J. Wang, H. Sepehri-Amin, H. Tajiri, T. Nakamura, K. Masuda, Y.K. Takahashi, T. Ina, T. Uruga, I. Suzuki, Y. Miura, K. Hono, Impact of carbon segregant on microstructure and magnetic properties of FePt-C nanogranular films on MgO (001) substrate, Acta Mater. 166 (2019) 413–423, https://doi.org/10.1016/j.actamat.2019.01.001.
[18] J.S. Chen, B.C. Lim, Y.F. Ding, G.M. Chow, Low-temperature deposition of L10 FePt films for ultra-high density magnetic recording, J. Magn. Magn. Mater. 303 (2006) 309–317, https://doi.org/10.1016/j.jmmm.2006.01.106.
[19] W.J. Boettinger, J.A. Warren, C. Beckermann, A. Karma, Phase-field simulation of solidification, Annu. Rev. Mater. Sci. 32 (2002) 163–194, https://doi.org/10.1146/annurev.matsci.32.101901.155803.
[20] C.E. Krill, L.Q. Chen, Computer simulation of 3-D grain growth using a phase-field model, Acta Mater. 50 (2002) 3057–3073, https://doi.org/10.1016/s1359-6454(02)00084-8.
[21] V. Vaithyanathan, L.Q. Chen, Coarsening of ordered intermetallic precipitates with coherency stress, Acta Mater. 50 (2002) 4061–4073, https://doi.org/10.1016/S1359-6454(02)00204-5.
[22] T. Koyama, Phase-field simulation microstructure formation in Ni-base superalloys, Int. J. Mater. Res. 101 (2010) 527–533. https://doi.org/10.3139/146.110306.
[23] T.M. Rogers, K.R. Elder, R.C. Desai, Numerical study of the late stages of spinodal decomposition, Phys. Rev. B 37 (1988) 9638–9649, https://doi.org/10.1103/PhysRevB.37.9638.
[24] T. Takaki, T. Hirouchi, Y. Tomita, Phase-field study of interface energy effect on quantum dot morphology, J. Cryst. Growth 310 (2008) 2248–2253, https://doi.org/10.1016/j.jcrysgro.2007.11.065.

[25] Y.U. Wang, Y.M. Jin, A.G. Khachaturyan, Phase field microelasticity modeling of surface instability of heteroepitaxial thin films, Acta Mater. 52 (2004) 81–92, https://doi.org/10.1016/j.actamat.2003.08.027.
[26] Y. Ni, L.H. He, A.K. Soh, Three-dimensional phase field simulation for surface roughening of heteroepitaxial films with elastic anisotropy, J. Cryst. Growth 284 (2005) 281–292, https://doi.org/10.1016/j.jcrysgro.2005.07.026.
[27] D.H. Yeon, P.R. Cha, S.I. Chung, J.K. Yoon, Phase field model for the dynamics of steps and islands on crystal surfaces, Met. Mater. Int. 9 (2003) 67–76, https://doi.org/10.1007/BF03027233.
[28] T. Koyama, H. Onodera, Modeling of microstructure changes in FePt nano-granular thin films using the phase-field method, Mater. Trans. 44 (2003) 1523–1528, https://doi.org/10.2320/matertrans.44.1523.
[29] L. Liu, L. Zhang, L. Liang, K. Ohsasa, T. Koyama, Q. Sheng, T. Hasegawa, S. Ishio, Microstructure of L10 FePt thin films with anisotropic interfacial energy coefficients and anisotropic atomic mobilities, J. Alloys Compd. 682 (2016) 176–179, https://doi.org/10.1016/j.jallcom.2016.04.261.
[30] Y. Ren, L. Liu, L. Liang, Q. Zheng, Y. Xu, L. Zhang, W.F. Rao, Influences of the substrate strain on microstructures of L10 FePt-X thin films by using phase field simulation, Mater. Today Commun. 32 (2022) 104123, https://doi.org/10.1016/j.mtcomm.2022.104123.
[31] J. Deng, H. Li, K. Dong, R.W. Li, Y. Peng, G. Ju, J. Hu, G.M. Chow, J. Chen, Lattice-mismatch-induced oscillatory feature size and its impact on the physical limitation of grain size, Phys. Rev. Appl 9 (2018) 34023, https://doi.org/10.1103/PhysRevApplied.9.034023.
[32] T. Takaki, T. Fukuoka, Y. Tomita, Phase-field simulation during directional solidification of a binary alloy using adaptive finite element method, J. Cryst. Growth 283 (2005) 263–278, https://doi.org/10.1016/j.jcrysgro.2005.05.064.
[33] S.Y. Hu, L.Q. Chen, A phase-field model for evolving microstructures with strong elastic inhomogeneity, Acta Mater. 49 (2001) 1879–1890, https://doi.org/10.1016/S1359-6454(01)00118-5.
[34] S. Yuasa, H. Miyajima, Y. Otani, Magneto-volume and tetragonal elongation effects on magnetic phase transitions of body-centered tetragonal FeRh 1–x Pt x, J. Phys. Soc. Japan. 63 (1994) 3129–3144, https://doi.org/10.1143/JPSJ.63.3129.
[35] Z. Feng, V.S. Babu, J. Zhao, M.S. Seehra, Effect of magnetic dilution on magnetic ordering in Ni p Mg1− p O, J. Appl. Phys. 70 (1991) 6161–6163, https://doi.org/10.1063/1.350030.
[36] P.W. Tasker, D.M. Duffy, The structure and properties of the stepped surfaces of MgO and NiO, Surf. Sci. 137 (1984) 91–102, https://doi.org/10.1016/0039-6028(84)90678-2.
[37] Y. Sumino, I. Ohno, T. Goto, M. Kumazawa, Measurement of elastic constants and internal frictions on single-crystal MgO by rectangular parallelepiped resonance, J. Phys. Earth 24 (1976) 263–273, https://doi.org/10.4294/jpe1952.24.263.
[38] M. Müller, P. Erhart, K. Albe, Thermodynamics of L 10 ordering in FePt nanoparticles studied by Monte Carlo simulations based on an analytic bond-order potential, Phys. Rev. B - Condens. Matter Mater. Phys. 76 (2007) 1–9, https://doi.org/10.1103/PhysRevB.76.155412.
[39] S. Hong, M.H. Yoo, Surface energy anisotropy of FePt nanoparticles, J. Appl. Phys. 97 (2005) 084315, https://doi.org/10.1063/1.1863424.
[40] A. Zebda, H. Sabbah, S. Ababou-Girard, F. Solal, C. Godet, Surface energy and hybridization studies of amorphous carbon surfaces, Appl. Surf. Sci. 254 (2008) 4980–4991, https://doi.org/10.1016/j.apsusc.2008.01.147.
[41] D. Turenne, A. Yaroslavtsev, X. Wang, V. Unikandanuni, I. Vaskivskyi, M. Schneider, E. Jal, R. Carley, G. Mercurio, R. Gort, N. Agarwal, B. Van Kuiken, L. Mercadier, J. Schlappa, L. Le Guyader, N. Gerasimova, M. Teichmann, D. Lomidze, A. Castoldi, D. Potorochin, D. Mukkattukavil, J. Brock, N.Z. Hagström, A.H. Reid, X. Shen, X.J. Wang, P. Maldonado, Y. Kvashnin, K. Carva, J. Wang, Y. K. Takahashi, E.E. Fullerton, S. Eisebitt, P.M. Oppeneer, S. Molodtsov, A. Scherz, S. Bonetti, E. Iacocca, H.A. Dürr, Nonequilibrium sub–10 nm spin-wave soliton formation in FePt nanoparticles, Sci. Adv. 8 (2022) 1–10, https://doi.org/10.1126/sciadv.abn0523.
[42] L. Zhang, Y.K. Takahashi, K. Hono, B.C. Stipe, J.Y. Juang, M. Grobis, FePtAg-C nanogranular film as thermally assisted magnetic recording (TAR) media, IEEE Trans. Magn. 47 (2011) 4062–4065, https://doi.org/10.1109/TMAG.2011.2157088.
[43] T. Henksmeier, P. Mahler, A. Wolff, D. Deutsch, M. Voigt;, L. Ruhm, A.M. Sanchez, D.J. As, G. Grundmeier, D. Reuter, Low-temperature fabrication of amorphous carbon films as a universal template for remote epitaxy, Commun. Mater. 5 (2024) 1–12, https://doi.org/10.1038/s43246-024-00718-7.
[44] J.W. Cahn, J.E. Hilliard, Free energy of a nonuniform system. I. Interfacial free energy, J. Chem. Phys. 28 (1958) 258–267, https://doi.org/10.1063/1.1744102.
[45] K. Nakajima, K. Kitahara, S. Ochiai, Calculation of stress concentration at the edge of island layer: demonstration for GaAs/Si, Japanese J. Appl. Physics, Part 1 Regul. Pap. Short Notes Rev. Pap. 35 (1996) 2605–2613, https://doi.org/10.1143/jjap.35.2605.
[46] I. Daruka, A.L. Barabási, Equilibrium phase diagrams for dislocation free self-assembled quantum dots, Appl. Phys. Lett. 72 (1998) 2102–2104, https://doi.org/10.1063/1.121289.
[47] I.M. Lifshitz, V.V. Slyozov, The kinetics of precipitation from supersaturated solid solutions, J. Phys. Chem. Solids 19 (1961) 35–50, https://doi.org/10.1016/0022-3697(61)90054-3.